PERGAMON

International Journal of Multiphase Flow 28 (2002) 579–596

International Journal of Multiphase Flow

www.elsevier.com/locate/ijmulflow

Experimental investigation of the velocity field induced by a Taylor bubble rising in stagnant water

R. van Hout *, A. Gulitski, D. Barnea, L. Shemer

Department of Fluid Mechanics and Heat Transfer, Faculty of Engineering, Tel-Aviv University, Tel-Aviv 69978, Israel

Received 13 May 2001; accepted 4 November 2001

Abstract

An experimental investigation of the flow field around a single Taylor bubble rising in a vertical pipe filled with stagnant water is presented. The Reynolds number of the flow based on the Taylor bubble rise velocity and the pipe diameter is 4350. The velocity field around the bubble was determined by Particle Image Velocimetry (PIV). The mean velocity fields in front of the bubble, in the liquid film, and in the wake region were calculated by ensemble-averaging the instantaneous velocity fields measured around 100 different bubbles. Ensemble-averaged velocities become negligible at $0.5D$ from the bubble nose and at $\sim$12 D from the bubble tail. However, notable instantaneous velocity fluctuations were found to exist up to $50D$ from the Taylor bubble tail. These residual vortices may influence the shape and the propagation velocity of the trailing bubble even at large separation distances.

Keywords: Taylor bubble; Two-phase slug flow; PIV

1. Introduction

Gas–liquid slug flow in pipes is one of the most complex flow patterns in two-phase flow. In vertical pipes the bulk of the gas is trapped inside large bullet-shaped (Taylor) bubbles that move upwards and are separated by liquid slugs that are sometimes aerated. The development of slug flow along the pipe is governed by the interaction between consecutive Taylor bubbles (Fabre et al., 1993; van Hout et al., 2001). The first experimental study of the coalescence mechanism between two consecutive Taylor bubbles was carried out by Moissis and Griffith (1962). It was found that the trailing bubble accelerates with decreasing separation distance and its nose sways from side to side. More recently, Pinto and Campos (1996) and Aladjem Talvy et al. (2000)

* Corresponding author.
E-mail address: rene@eng.tau.ac.il (R. van Hout).

0301-9322/02/$ - see front matter
PII: S0301-9322(01)00082-9

studied bubble coalescence using pressure transducers and image processing technique, respectively. In these experiments, only the bubble interface velocities were determined and no information on the velocity field in the liquid slug separating the bubbles was obtained.

It is generally assumed that the trailing bubble nose is affected by the velocity field in the liquid phase ahead of it (Shemer and Barnea, 1987; Polonsky et al., 1999b). Information on the velocity field in the wake of the leading bubble is therefore indispensable for the understanding of the trailing bubble movement.

However, available data on the velocity field around elongated bubbles in pipes are very limited. It is therefore instructive to consider also measurements in turbulent wakes of solid bluff bodies in pipes. Taylor and Whitelaw (1984) applied Laser Doppler Velocimetry to study the effect of blockage ratio and geometry on the velocity characteristics and wall pressure for axisymmetric turbulent flow. It was observed that both the wake length and the maximum axial centerline velocities increase with increasing blockage ratio. Maximum turbulent intensities occurred near the rear stagnation point at a radial position corresponding to the bluff body's edge.

The boundary conditions around a Taylor bubble are quite different from a solid body. Beyond the absence of the non-slip condition at the bubble surface, one of the most striking differences is the oscillation of the bubble bottom. Polonsky et al. (1999a) performed a study of the oscillatory motion of the tail of a Taylor bubble rising in stagnant and upward flowing water in a vertical pipe of 25 mm internal diameter (ID). The amplitude of the oscillations increases with the bubble length, whereas the frequency remains nearly constant, approximately 4 Hz. The oscillating nature of the bottom influences the vortex structure in the wake. Tokuhiro et al. (1998) measured the turbulent flow past an oscillating air bubble and a solid ellipsoid by Particle Image Velocimetry (PIV). It was found that differences between the solid and the bubble were confined to the near wake region, up to $2D$ behind the bubble, where D is the equivalent bubble diameter. For strongly inclined tail interfaces, wake symmetry was lost and the wake was characterized by a single vortex. Maximum r.m.s. values of the fluctuating velocities were located at $r/D = 0.5$ for both solid and bubble. The r.m.s. values were lower for the bubble than for the solid.

Measurements of flow field parameters around elongated bubbles in pipes are sparse (Kvernvold et al., 1984; Nakoryakov et al., 1986, 1989; Shemer and Barnea, 1987; DeJesus et al., 1995; Kawaji et al., 1997; Ahmad et al., 1998; Polonsky et al., 1999b). Kvernvold et al. (1984) performed velocity measurements in horizontal slug flow using Laser Doppler Velocimetry. The length of the wake region increased with increasing Reynolds number (Re) based on the mixture velocity. Nakoryakov et al. (1986, 1989) investigated the velocity field in vertical upward continuous slug flow using an electrochemical method. Both velocity and wall shear stress measurements were carried out. The Taylor bubble wake length was found to be independent of the liquid flow rate and was approximately $2D$ for all cases, where D is the pipe diameter. The axial centerline velocity in the liquid slug exhibited a maximum at approximately $1D$ from the bubble tail. Intensive turbulent fluctuations were observed in the region where the annular jet mixes with the flow in the wake. The axial fluctuating velocity component was larger than for single phase turbulent pipe flow. Shemer and Barnea (1987) applied a hydrogen bubble technique to visualize the instantaneous velocity profiles behind an elongated bubble moving in 20 mm ID vertical and horizontal glass tubes in co-current flowing water. The observed velocity profile was highly distorted in the near wake of the bubble and seemed to be fully developed at approximately $12D$ from the tail of the bubble. Ahmad et al. (1998) applied a photochromic dye activation technique

to measure the instantaneous velocity profiles in the near wall region around individual and coalescing pairs of Taylor air bubbles rising in a 25.6 mm ID tube filled with stagnant kerosene. At approximately $2D$ behind the bubble tail, large vortices decayed and the flow tended to become stagnant again. Polonsky et al. (1999b) determined the velocity field in front of a Taylor bubble rising in stagnant and upward flowing water using PIV. In stagnant water, far upstream ($>10D$) of the bubble nose, non-zero velocities, ranging between 1 mm/s for short bubbles ($2.5D$) to 3 mm/s for longer bubbles ($9.0D$), were detected due to bubble expansion. The onset of reversed flow occurred at approximately $0.66D$ in front of the bubble, this distance decreasing with increasing liquid flow rate. Velocities in the falling liquid film around the bubble were determined by particle streaks. In all cases the flow in the liquid film was laminar over the whole bubble length.

In the present work the detailed velocity characteristics of the complete flow field around a Taylor bubble rising in stagnant water in a vertical pipe is studied using PIV. The relation between the instantaneous velocity field and the movement of the trailing elongated bubble is discussed.

2. Experimental facility and data processing

2.1. Experimental facility

Experiments were carried out in a transparent (Perspex), 4 m long vertical pipe with 25 mm ID. Measurements were performed at a distance of 2 m from the inlet. At the measuring station the pipe was surrounded by a rectangular transparent Perspex box filled with water in order to reduce image distortion. To estimate the effect of the small difference in refractive index between water and Perspex, a ruler was inserted into the center-plane of the test pipe and imaged. Only the measurement point closest to the pipe wall was found to be somewhat affected by distortion.

In the present study, a large water tank was filled by tap water, filtered by a particle filter. A small amount of almost neutrally buoyant (specific gravity 0.95) polystirol particles, 20–40 μm in diameter, was added to the water. The particles contain fluorescent dye and emit light in the yellow-orange region of the spectrum (572–594 nm) when illuminated by a laser (Laser-Induced Fluorescence). At the beginning of each experimental run, the pipe was refilled with water and sufficient time elapsed between consecutive experimental runs to ensure that residual flow disturbances were negligible. Air was injected at a pressure of 0.4 bar through a computer-controlled injection valve, thus producing Taylor bubbles of any desired length. In this study the average bubble length was $3.6D \pm 0.3D$. More details on the experimental facility and the bubble injection procedure are given in Polonsky et al. (1999a).

2.2. Measurement technique

The velocity field in the liquid around the Taylor bubble was determined by PIV. In the present research, a pulsed Nd:YAG MiniLase III PIV-15 laser was used as the illumination source. A vertical laser sheet was generated at the pipe axis by a spherical and a cylindrical lens. The sheet thickness was about 1mm at the measurement position. The two laser heads produced a pair of short (5–7 ns) pulses at a wavelength of 532 nm (green light) with a total energy of 50 mJ/pulse. A KODAK ES 1.0 CCD camera (8 bit Monochrome, progressive scan interline transfer) with a

maximum frame rate of 30 fps (dual-channel mode) was used. The camera resolution is 1008 × 1018 pixels. The camera was operated in triggered double exposure mode which allowed capturing of a pair of two single pulsed frames at a short time interval. The images were digitized using a Road Runner frame grabber board that saved the images in the RAM of a computer. Commercially available Video Savant software (IO-industries) was used for displaying and capturing the images. A high-pass filter (>550 nm) was placed on the camera objective lens to filter out the green laser light (532 nm) from the images. The images therefore only contain fluorescent particles seen as bright dots. An example of a PIV image is shown in Fig. 1. The bottom part of the Taylor bubble, including a part of the near wake and the film region, can be clearly seen. Two small bubbles can be discerned near the Taylor bubble bottom. Note the highly irregular instantaneous shape of the Taylor bubble tail.

An external synchronizer unit, controlled by dedicated software, was used to synchronize the different components of the measuring system. An optical sensor located on the pipe upstream of the measuring location, triggered the synchronizer upon the passage of the bubble nose. The synchronizer then generated a trigger signal at the desired frequency (maximum 14 Hz in the present research) to both the camera and the frame grabber. Upon receiving the trigger signal, the camera returned a pulse to the synchronizer unit that in turn triggered the two laser heads at a specified time delay between the laser pulses. Each illumination pulse was captured by the camera on a different frame and the resulting image (1008 × 2036 pixels) contained a pair of frames (each

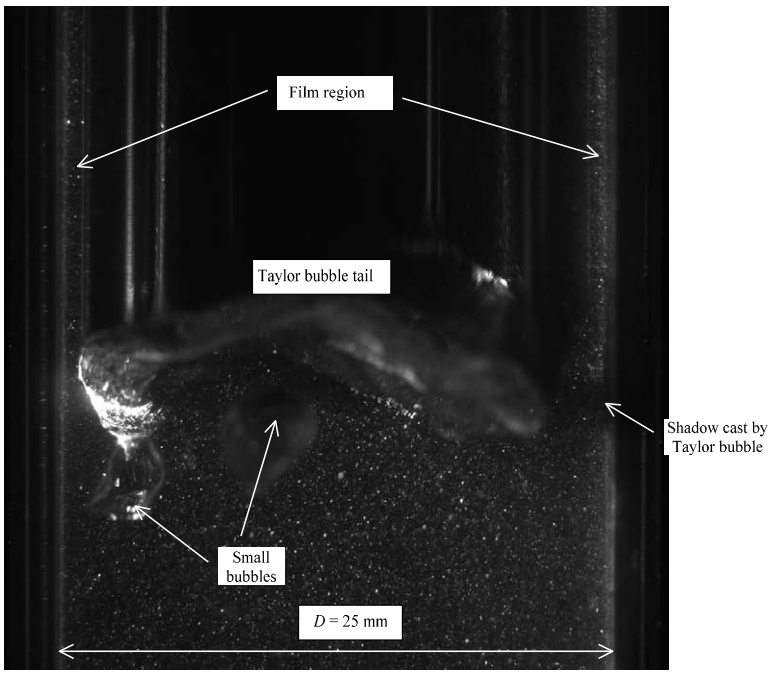

Fig. 1. An image of the Taylor bubble bottom, the near wake and the film region. Bright dots in the liquid region represent the fluorescent particles.

1008 × 1018 pixels). In this way a series of images could be captured. The number of consecutive images is limited only by the available RAM size.

The velocity magnitudes in the flow field under investigation range from O (1 mm/s) to O (1 m/s). The time delay between the laser pulses was selected so that the maximum particle displacement between the frames in each pair did not exceed about 16 pixels. Different time delays between laser pulses were selected and adjusted to the velocity magnitudes expected in each particular region of the flow field around the bubble. As the time delay between the laser pulses in each pair is small compared to the flow time scales, instantaneous velocity maps in the illuminated plane can be obtained by applying a direct cross-correlation technique to the image pairs (Adrian, 1991; Roth and Katz, 1999). Each image was divided into interrogation regions of 32 by 32 pixels, with 50% overlap (spatial resolution 16 pixels). Measurements performed with a field of view of 30 mm × 30 mm (spatial resolution of approximately 0.5 mm) produced erroneous results in the vicinity of the wall in the near wake and film region due to high velocity gradients in this area. Therefore additional measurements were carried out with a field of view of 12 mm × 12 mm (spatial resolution of approximately 0.2 mm) near the pipe wall in the film region and in the near wake region (up to 1D from the bubble bottom). Fig. 2. demonstrates the measured radial distributions of the axial velocity component in the wake of the bubble at $x/D = 0.25$, ensemble-averaged over 100 individual bubble injections for the two spatial resolutions. Near the wall, the high spatial resolution enables an accurate determination of the penetrating liquid film velocities, while away from the wall, results obtained for both fine and coarse resolution collapse onto a single curve.

2.3. Data processing

At each time delay between two laser pulses, 100 bubbles were injected and the instantaneous velocity fields around them were determined. In turbulent flow, the instantaneous velocity vectors can be decomposed into a mean, $\bar{\boldsymbol{U}}(\boldsymbol{x}, r)$ and a random fluctuating component $\boldsymbol{u}'(\boldsymbol{x}, r)$:

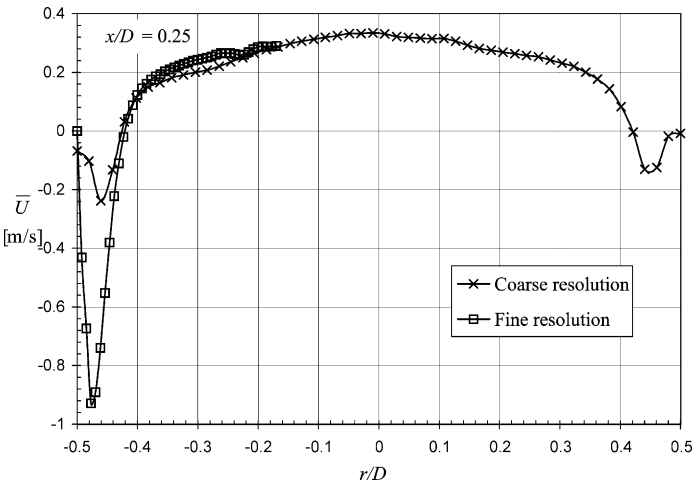

Fig. 2. Comparison of the axial velocity profiles calculated from the coarse and the fine resolution PIV images.

$$\boldsymbol{U}(\boldsymbol{x},r) = \bar{\boldsymbol{U}}(\boldsymbol{x},r) + \boldsymbol{u}'(\boldsymbol{x},r). \tag{1}$$

The mean radial and axial velocity components around a bubble were determined by ensemble averaging the N measured instantaneous velocity fields

$$\bar{\boldsymbol{U}}(\boldsymbol{x},r) = \frac{1}{N}\sum_{1}^{N} \boldsymbol{U}(\boldsymbol{x},r). \tag{2}$$

In the present research, the axial dimensionless coordinate x/D is taken relative to the bubble nose ahead of the bubble, and relative to the bubble bottom in the wake region. The corresponding coordinate in the radial direction is r/D.

3. Experimental results

3.1. Vector plot of the mean velocity field around a Taylor bubble

In Fig. 3 the vector plot of the mean velocity field around a Taylor bubble rising in stagnant water is shown. The spatial resolution in the plots was reduced for better visibility. Fig. 3(a) shows the region in front of the bubble nose and part of the initial film formation zone, while in Figs. 3(b) and (c), the bottom area of the falling liquid film and the wake region are shown. The effect of the bubble movement is negligible beyond a distance of about $0.5D$ ahead of its nose. However, small expansion-induced velocities upstream of the bubble nose of the order of 1.5 mm/s were detected in the present measurements, in agreement with Polonsky et al. (1999b).

Upon approaching the bubble nose, the axial centerline velocity increases and flow reversal occurs near the pipe wall at approximately $0.5D$ from the bubble tip. This agrees with Polonsky et al. (1999b). The liquid film is accelerated along the bubble as its thickness diminishes. The falling film velocity does not reach its terminal value (when gravity forces are balanced by shear forces) due to the relatively short bubble length. The film enters the liquid slug as an annular jet creating a toroidal vortex stretching up to $2D$ in the near wake of the bubble (Fig. 3(b)). A much weaker vortex with an opposite sense of rotation can be observed in Fig. 3(c) between $2 < x/D < 4$. As expected, the mean velocity field exhibits axial symmetry.

3.2. Mean velocity profiles $\bar{U}(x,r)$ and $\bar{V}(x,r)$

The continuity equation can serve to test the accuracy of the measured mean velocity fields. Assuming that the mean velocity field measured at the centerline plane of the pipe is two-dimensional, the continuity equation can be written as

$$r\frac{\partial}{\partial x}\bar{U} + \frac{\partial}{\partial r}r\bar{V} = 0. \tag{3}$$

In Fig. 4 both terms in (3), calculated at different axial distances from the bubble nose and at various radial locations, are presented. This plot was obtained by differentiating the experimentally obtained mean velocity profiles, a procedure that inevitably reduces the accuracy. Maximum deviations from the continuity equation exist in the regions with high velocity gradients. Still, it

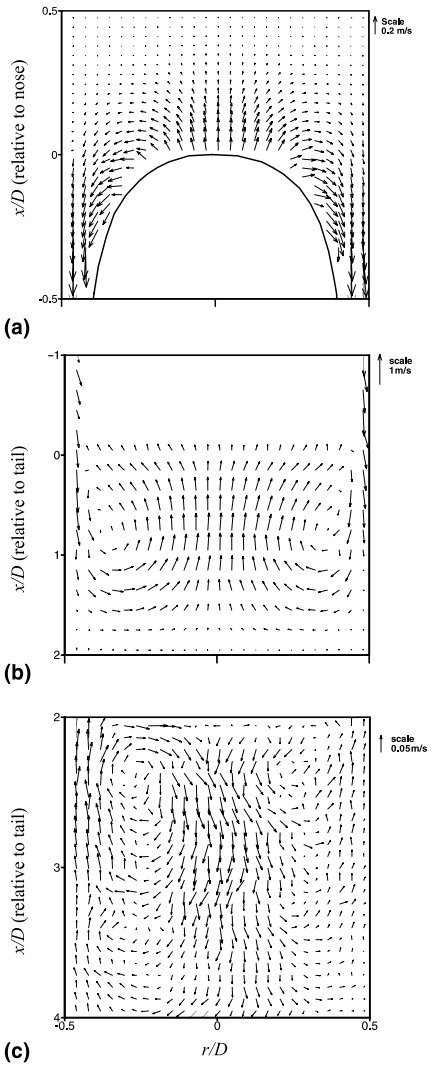

Fig. 3. Ensemble-averaged velocity vector plots around the Taylor bubble: (a) in front of the bubble, (b) in the liquid film and in the near wake region, (c) away from bubble.

can be seen that the measured spatial distributions of the two velocity components satisfy the continuity equation reasonably well.

The radial profiles of the ensemble averaged axial $\bar{U}(x,r)$ and radial $\bar{V}(x,r)$ velocity components at different positions x/D (measured from the bubble nose) are depicted in Figs. 5(a) and (b), respectively. Since all mean velocity profiles exhibit axial symmetry, the results are averaged over the left and right sides of the profile (effectively doubling the ensemble size) and thus presented for the range of $0 < r/D < 0.5$. Close to the bubble tip ($x/D = 0.06$), the axial velocity component at the centerline ($r/D = 0$) approaches the bubble drift velocity $U_d = 0.174$ m/s, as expected from continuity. For all axial locations in Fig. 5(a), the radial location for velocity

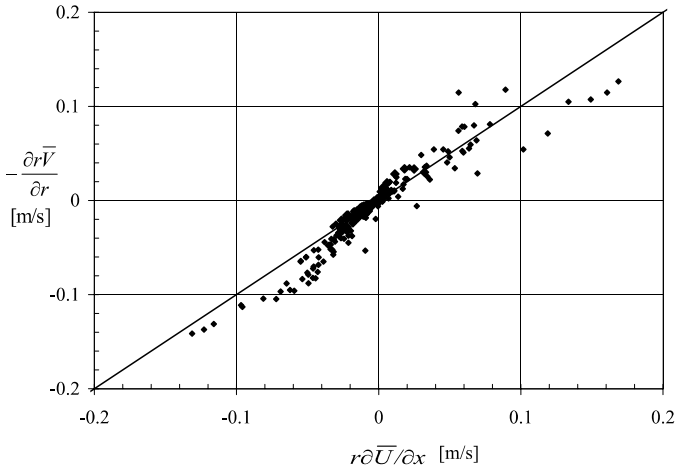

Fig. 4. Comparison of the two terms in the continuity equation (3), measured in front of the Taylor bubble.

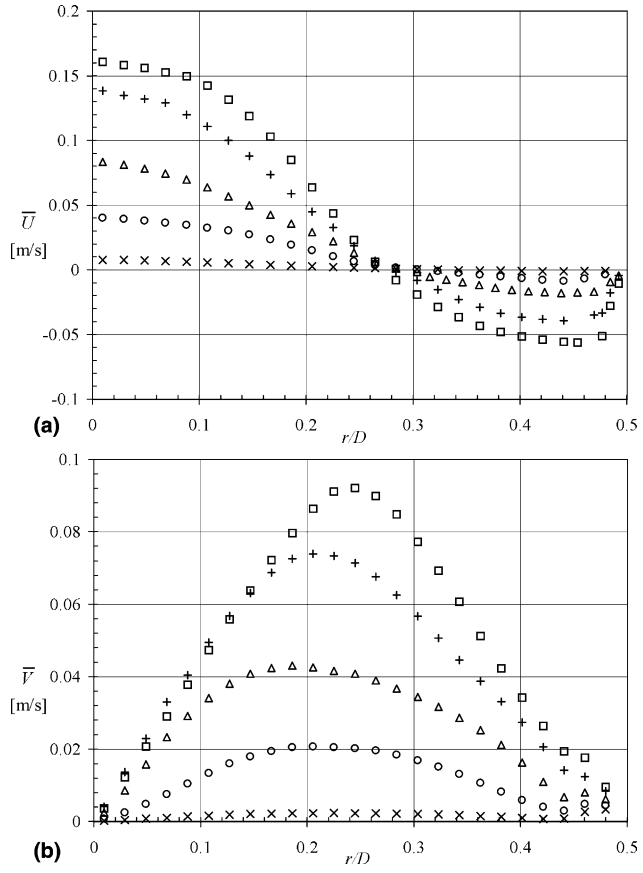

Fig. 5. Radial distributions of the ensemble averaged velocity components at various distances ahead of the Taylor bubble nose: (a) axial component, (b) radial component. □: $x/D = 0.06$; +: $x/D = 0.1$; △: $x/D = 0.2$; ○: $x/D = 0.3$; ×: $x/D = 0.5$.

reversal lies between $0.25 < r/D < 0.3$. The onset of the reverse flow occurs at about $x/D = 0.5$ before the bubble tip. At $x/D = 0.06$, close to the entrance to the film region, the negative velocity attains values exceeding 5 cm/s. The radial velocity component $\bar{V}$ in front of the bubble is positive at all locations, i.e. directed from the axis towards the pipe wall. The maximum values of $\bar{V}$ are somewhat lower than those of the axial velocity $\bar{U}$.

The velocity distribution in the liquid film region is studied in Fig. 6. In Fig. 6(a) the bubble shape is plotted together with the velocity profiles at various axial distances x/D from the bubble tip. Detailed analysis of the measured bubble shape and comparison to a predictive model were presented in Polonsky et al. (1999a) and are not considered here. All velocity profiles are plotted using the same scaling and shifted according to their relative axial location, so that the velocity values at the pipe wall vanish. Within the liquid film, the velocity profiles exhibit zero shear stress at the bubble interface. At the exit of the film region, it is difficult to estimate the velocities close to the bubble interface due to bubble bottom oscillations. Fig. 6(b) depicts the variation of the maximum downward axial velocity within the liquid film as a function of the axial distance from the bubble nose. These velocities attain values of approximately 1 m/s at the exit from the film. For bubble lengths of about $3.6D$ studied here, the film velocity is below the terminal value of a

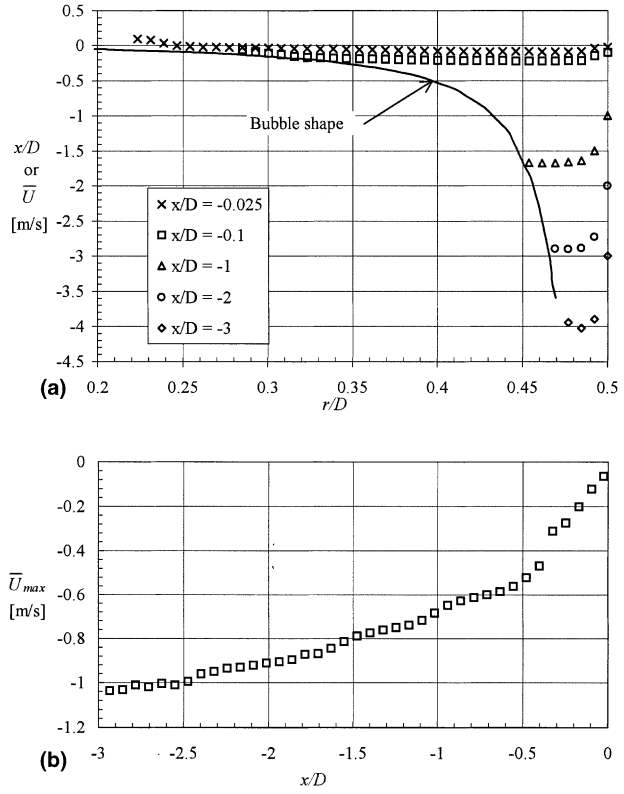

Fig. 6. Liquid film area: (a) The bubble interface and the radial profiles of the axial velocity, shifted according to the distance from the bubble tip; (b) variation of the maximum axial cross-sectional velocity along the film.

free falling film balanced by the shear at the wall. The measured results are in agreement with Ahmad et al. (1998) and Polonsky et al. (1999b).

Radial distributions of the ensemble-averaged axial velocity component, $\bar{U}$, in the bubble wake are presented in Fig. 7. Since the absolute values of $\bar{U}$ vary considerably with the distance x/D from the bubble bottom, the distributions in the immediate vicinity of the bubble ($0 < x/D < 1.8$, Fig. 7(a)) and at some distance from it ($2.0 < x/D < 5.0$, Fig. 7(b)) require different scaling. In Fig. 7(a), the axial velocity is directed upward in the central region of the pipe, while the flow direction is downward closer to the wall. In Fig. 7(b), the axial velocity component changes sign, becoming negative in the center of the pipe and positive closer to the wall. At the entrance to the wake region ($x/D = 0.06$), the axial velocity is distributed nearly uniformly behind the whole bubble cross-section, and has a value that approaches the drift velocity of the bubble, $U_d = 0.174$ m/s. Near the wall, the velocity changes direction and the profile attains a shape typical for a downward falling annular jet. This annular jet is quickly absorbed into the bulk of the liquid in the wake and its maximum absolute velocity decreases from about 1 m/s at $x/D = 0.06$ to close to zero at $x/D = 1.8$, while the whole jet area widens. Mass conservation was checked for the

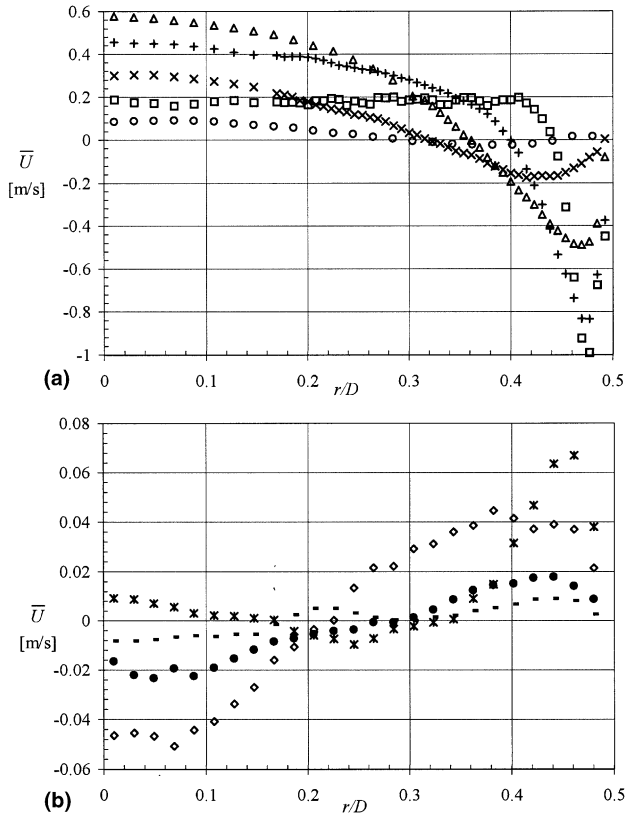

Fig. 7. Radial distributions of the ensemble-averaged axial velocity components at various distances from the Taylor bubble bottom: (a) near wake region, (b) $2.0 \leqslant x/D \leqslant 5.0$. □: $x/D = 0.06$; +: $x/D = 0.5$; △: $x/D = 1.0$; ×: $x/D = 1.5$; ○: $x/D = 1.8$; ∗: $x/D = 2.0$; ◇: $x/D = 3.0$; ●: $x/D = 4.0$; ■: $x/D = 5.0$.

measured liquid velocity profiles. The total flow rate at each axial cross-section remains close to zero, so that the mean cross-sectional velocity remains well below 5% of the maximum local mean velocity.

The variation of the ensemble-averaged axial velocity, $\bar{U}$, at the pipe centerline is shown in Fig. 8 as a function of the distance from the bubble (i.e. from the bubble nose ahead of the bubble and from the bubble tail in the wake region). Note that at the bubble interface, the axial velocity component equals U_d, as already noticed in Figs. 5(a) and 7(a). The velocity in front of the bubble decreases fast and vanishes at $x/D > 0.5$ with the exception of expansion-induced velocities. In contrast, the centerline axial velocity in the bubble wake increases initially from U_d to about 0.6 m/s at $x/D \approx 1$, then decreases fast, crosses the x-axis at $x/D = 2D$ and becomes negative (downward direction) with a maximum absolute value of about 0.05 m/s at $x/D \approx 2.5$. These results are in general agreement with the experiments of Nakoryakov et al. (1986, 1989) in continuous slug flow. For $x/D > 5$ the axial velocity at the centerline becomes positive again, attains a local maximum at about $x/D = 6$ and then slowly decreases to zero at larger distances from the bubble. The change of sign of the axial velocity at the center line reflects the sequence of vortex rings with opposite sense of rotation which exists in the wake and is clearly seen on the vector plots of Fig. 3(b) and (c). This might explain the trailing bubble slowing down with respect to the leading bubble as reported by Fagundes Netto et al. (1998) in horizontal slug flow.

The radial profiles of the ensemble averaged radial velocity component $\bar{V}$ are shown in Fig. 9. The absolute values of the radial velocities are notably lower than the corresponding axial velocity component and never exceed 0.1 m/s. The sign of the radial velocity component at various locations in the near wake region is in agreement with the vortex pattern presented in Fig. 3(b). The radial velocity component becomes negligible at about $x/D > 2$.

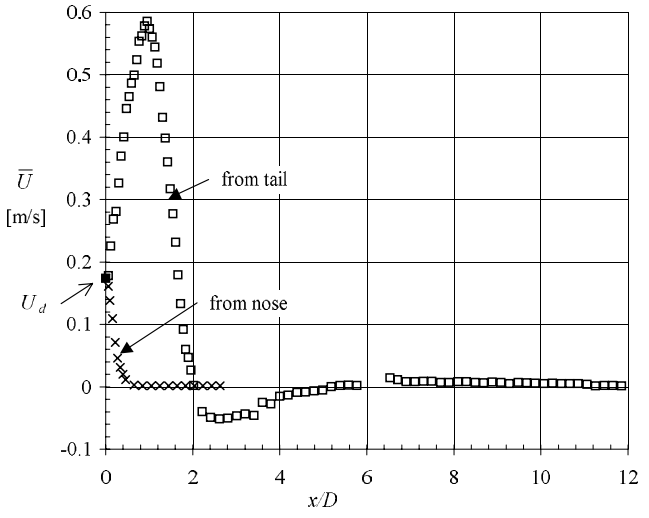

Fig. 8. The variation of the ensemble averaged axial velocity at the centerline of the pipe as a function of the distance from the Taylor bubble nose and tail.

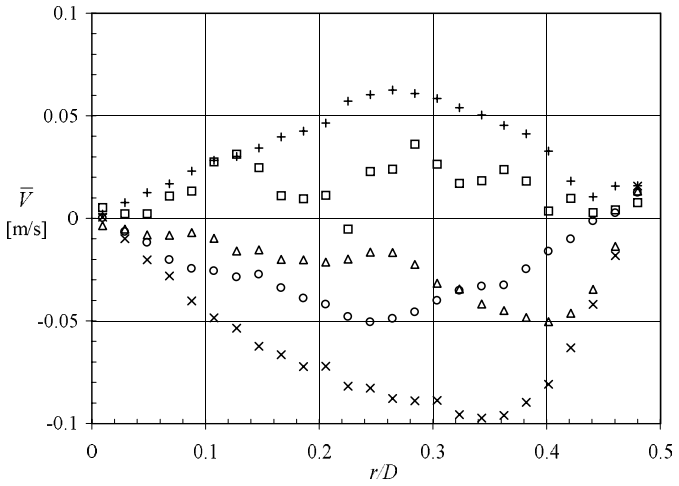

Fig. 9. Radial distributions of the ensemble-averaged radial velocity component at various distances from the Taylor bubble bottom. □: $x/D = 0.06$; +: $x/D = 0.5$; △: $x/D = 1.0$; ×: $x/D = 1.5$; ○: $x/D = 1.8$.

3.3. Instantaneous velocity field behind the Taylor bubble

The mean velocities in the wake of the bubble decay fast and effectively vanish at a relatively short distance ($x/D > 12$) from the bubble tail. However, instantaneous velocities remain noticeable even at large distances behind the bubble. An example of instantaneous realizations of the velocity field is given in Fig. 10 at different axial positions x/D. In Fig. 10(a), small-scale vortices created by the turbulent mixing process in the near wake region of the bubble are detected at $x/D \approx 6$. Due to vortex pairing and viscous dissipation, the small-scale vortices disappear; see Figs. 10(b)–(d). Far from the bubble tail, at $x/D \approx 30$ and $x/D \approx 50$, two distinct vortices with a length scale of the internal pipe diameter turning in clockwise and anti clockwise direction, can be distinguished in Figs. 10(c) and (d). The vortex centers do not move much in stagnant water and their development in time can be observed. It is assumed here that these large vortices are related to the bubble bottom oscillations and become visible in the far wake, after the much stronger, small-scale vortices generated by the turbulent mixing process in the near wake, decay. In each bubble bottom oscillation period, two large-scale vortices with opposite senses of rotation are generated. Note that the distance between the successive vortex cores in Figs. 10(c) and (d) is somewhat less than $1D$. Since the translational velocity of the Taylor bubble is about $7D$/s (0.174 m/s), this distance between the vortex centers is consistent with the observed frequency of the bubble bottom oscillations, which is about 4 Hz (Polonsky et al., 1999a). It therefore appears that the flow field in the near wake is dominated by the turbulent mixing process due to the penetrating wall jet, similar to the case of a solid body wake (Taylor and Whitelaw, 1984). In contrast to that, at $x/D \approx 30$ and 50, Figs. 10(c) and (d), the flow field is characterized by residual vortices created by the quasi-periodic oscillations of the bubble tail.

It is commonly speculated that the tip location and the translational velocity of the elongated bubble in slug flow are affected by the local instantaneous maximum velocity in the liquid slug just ahead of the bubble. It is therefore instructive to examine the variation of the local instantaneous

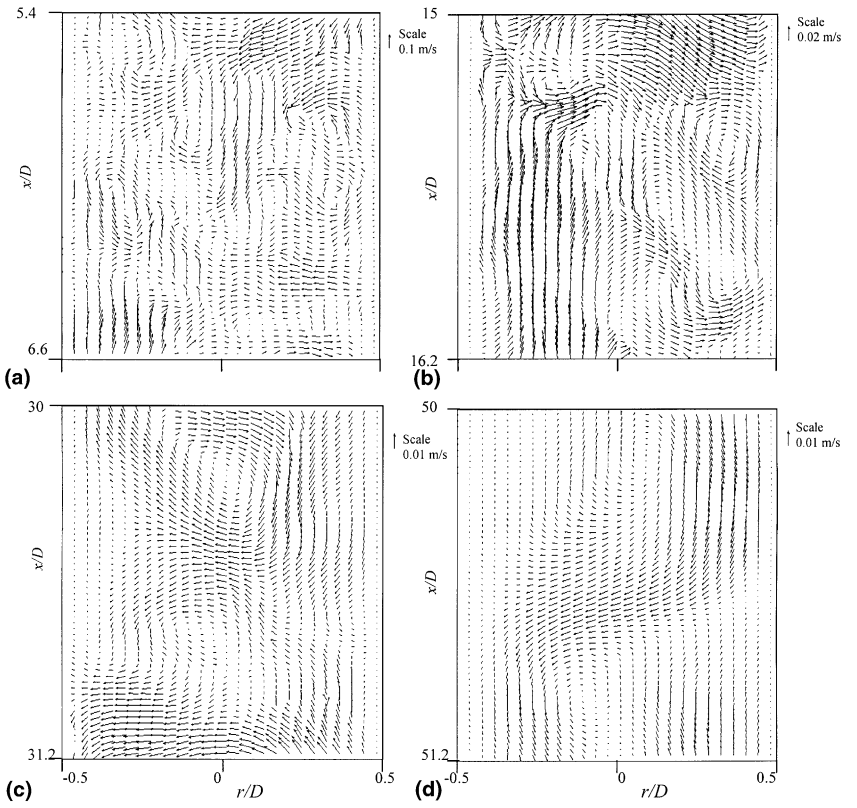

Fig. 10. Vector plots of the instantaneous velocity field at various locations behind the bubble.

maximum velocity $U_{\max}$ as a function of the distance x/D from the bubble bottom. For each injected bubble and axial cross-section x/D, the local instantaneous $U_{\max}$ was determined and ensemble averaged. The variation of $\bar{U}_{\max}$ with x/D is presented in Fig. 11. The error bars indicate the standard deviation ($\pm 2\sigma$) of the measured values at some axial locations. Note that in contrast to $\bar{U}$ at the center-line (Fig. 8) that essentially vanishes for $x/D > 12$, $\bar{U}_{\max}$ at this location is of the order of a few cm/s and decays much slower. Even at x/D approaching 50, $\bar{U}_{\max}$ is only slightly below 0.5 cm/s. This fact can account for the non-zero relative approach velocities of the trailing bubble at considerable distances from the leading one as observed by Aladjem Talvy et al. (2000).

Fig. 12 presents histograms of the distributions of the radial locations r/D of the local maximum velocity $U_{\max}$ for different axial positions. Close to the bubble tail, at $2 < x/D < 3$, maximum velocities occur mostly near the pipe centerline, whereas at $3 < x/D < 5$ they are located close to the pipe wall at $|r/D| \approx 0.4$. This may explain the observed strong swaying of the trailing bubble tip in the wake of the leading bubble at these separation distances (Aladjem Talvy et al., 2000). At larger distances from the bubble tail ($20 < x/D < 30$), no preferred radial position can be discerned.

In Fig. 13 the radial profiles of the r.m.s. values of $u'(x,r)$ and $v'(x,r)$ are shown at different axial positions from the bubble tail. The data were axially averaged over $0.1D$, increasing the effective ensemble size. The high values of u' immediately below the bubble bottom, at $x/D = 0.06$,

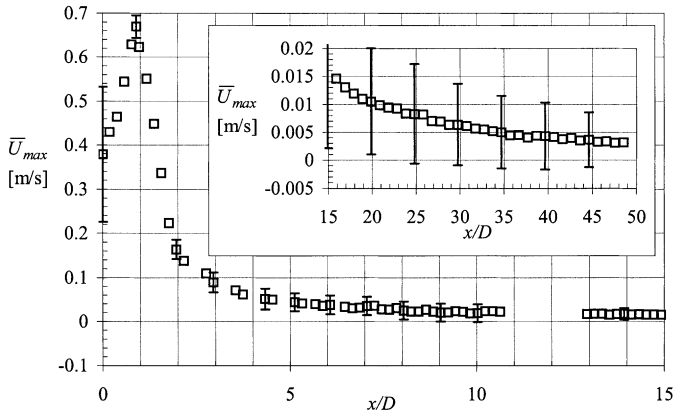

Fig. 11. The dependence of the ensemble-averaged instantaneous maximum velocity in the cross-section as a function of the distance from the bubble bottom.

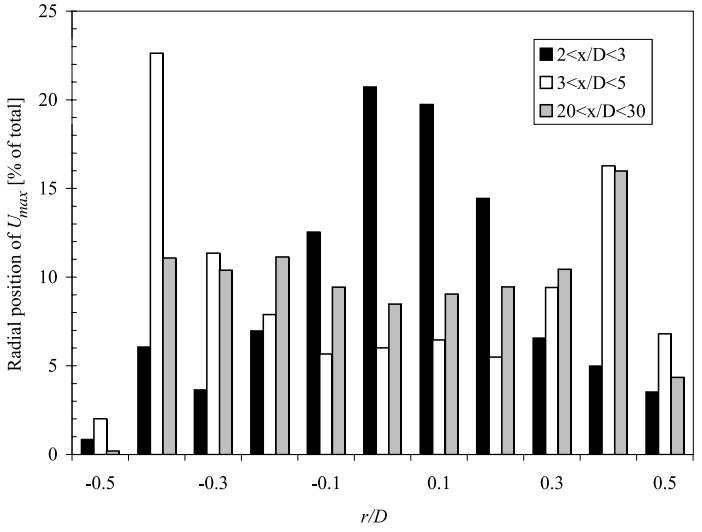

Fig. 12. Histograms of the distribution of the radial location of $U_{\max}$ for various distances from the bubble bottom.

reflect the vigorous oscillations of the bubble bottom interface (cf. Fig. 1). The maximum of u' is attained close to the pipe wall in the free shear layer between the penetrating annular wall jet and the recirculating flow in the near wake. This is in agreement with the radial distribution of turbulent intensities behind a bluff body confined by a pipe (Taylor and Whitelaw, 1984), around a small bubble (Tokuhiro et al., 1998) as well as in continuous slug flow (Nakoryakov et al., 1986, 1989). The values of u' further away from the bubble are related to the local center-line velocity, Fig. 8. These values attain a local maximum at $x/D \approx 1$, and then decay. The near-wall peak of the distributions gradually flattens, reflecting the absorption of the jet in the liquid, cf. Fig. 7. Qualitatively, the shape of the u' profiles resembles that of a fully developed turbulent flow in a circular pipe (Laufer, 1953). It should be stressed, however, that the mean liquid flow rate in the

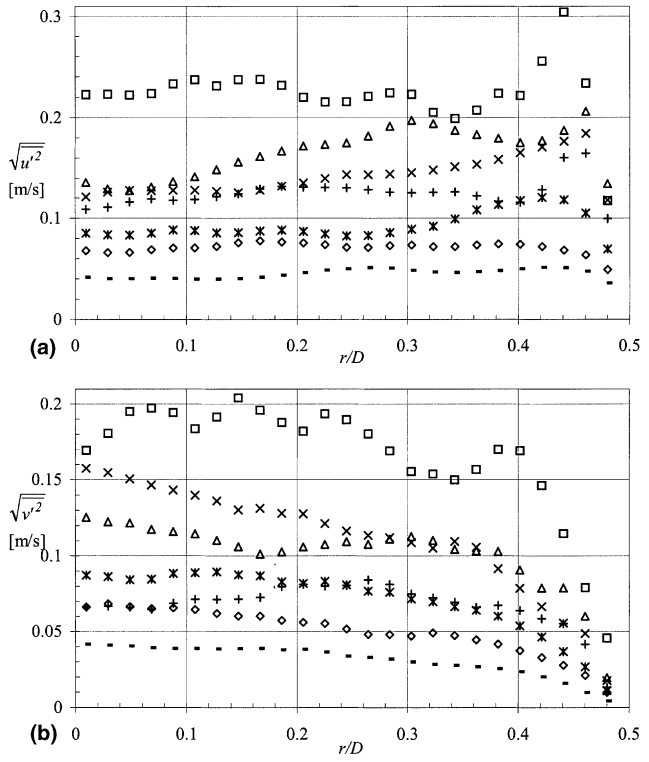

Fig. 13. Radial distributions of the r.m.s. values of the velocity component fluctuations for various distances from the bubble bottom: (a) axial component u', (b) radial component v'. □: $x/D = 0.06$; +: $x/D = 0.5$; △: $x/D = 1.0$; ×: $x/D = 1.5$; ∗: $x/D = 2.0$; ◇: $x/D = 3$; ▬: $x/D = 5.0$.

present experiments is zero, and that the turbulence resulting from the mixing process in the wake cannot be sustained at larger distances from the bubble bottom. In the near wake region, the characteristic Reynolds number $Re = U_d D/\nu = 4350$, based on the bubble drift velocity U_d and the kinematic viscosity of water ν.

The r.m.s values of the radial velocity fluctuations, v', Fig. 13(b), at each axial cross-section are of the same order of magnitude as the corresponding values of u', in agreement with Taylor and Whitelaw (1984). This can be attributed to the vortical nature of the flow in the near wake as evident from Fig. 10(a).

The radial distributions of the ensemble-averaged Reynolds shear stress $\overline{u'v'}$ in the near wake region are plotted in Fig. 14(a). The values of $\overline{u'v'}$ initially increase, attain a maximum at $1 < x/D < 1.5$, and then decay. The maximum is observed around $r/D = 0.25$. The radial distributions of the cross-correlation coefficient $\overline{u'v'}/(\sqrt{\overline{u'^2}}\sqrt{\overline{v'^2}})$, plotted in Fig. 14(b), attain a maximum of about 0.6 at $x/D = 1.5$ and r/D around 0.25. These values are somewhat higher than those observed in turbulent pipe flow. The fast decay in the cross-correlation coefficient represents the laminarization of the flow in the wake for $x/D > 2$. Already at $x/D = 3$, fluctuations in the axial and the radial direction, while still existing, are not correlated anymore and do not contribute to the momentum transfer. The flow can therefore be considered turbulent only for $x/D < 2$.

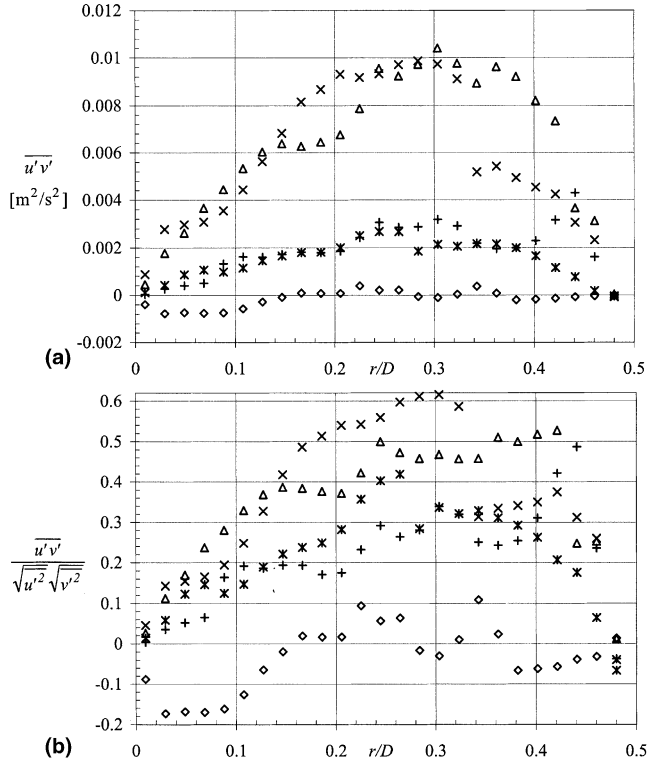

Fig. 14. Radial distributions of the Reynolds shear stresses $\overline{u'v'}$ for various distances from the bubble bottom: (a) absolute values, (b) cross-correlation coefficients. +: $x/D = 0.5$; △: $x/D = 1.0$; ×: $x/D = 1.5$; ∗: $x/D = 2.0$; ◇: $x/D = 3.0$.

4. Summary and conclusions

Detailed measurements of the flow field around a Taylor air bubble rising in stagnant water in a vertical pipe were carried out. A series of 100 single bubbles with a length of $3.6D$ were injected into a 4 m long pipe with internal diameter $D = 25$ mm. The Reynolds number of the flow in the near wake region equaled 4350. Velocity field measurements were carried out by PIV in front of the bubble, in the liquid film and in the wake of the bubble. Memory limitations dictated the choice of the maximum ensemble size. However, the mean distributions of both velocities and turbulent quantities did not differ notably for ensemble sizes ranging from 70 to 100.

The effect of the bubble movement on the liquid ahead of it is restricted to $x/D < 0.5$. The falling liquid film around the Taylor bubble is accelerated up to a maximum velocity of about 1 m/s at the film exit. The downward annular liquid film mixes with the upward flowing liquid immediately below the bubble bottom and generates a complicated turbulent flow pattern in the near wake region for $x/D < 2$. The averaged velocity map shows a distinct toroidal vortex pattern. Mean axial velocities for $x/D < 2$ are directed upward at the centerline and downward near the pipe circumference. For $2 < x/D < 5$, the averaged velocity map reveals a secondary, much

weaker toroidal vortex with an opposite sense of rotation. Mean velocities decay further with increasing x/D and become negligible for $x/D > 12$.

In contrast to the ensemble-averaged velocities, the instantaneous velocities remain detectable up to the last measuring location of about $50D$. The instantaneous velocity field in the near wake region is characterized by small-scale vortices and high local velocities. The small-scale structure of the flow gradually decays. For $x/D > 25$, only vortices of the scale of the pipe diameter survive and the separation distance between consecutive vortices may be related to the characteristic frequency of the bubble bottom oscillations.

The analysis of the instantaneous and the mean velocity fields in the Taylor bubble wake sheds light on the behavior of a trailing Taylor bubble propagating in the wake of a leading one, as reported by Aladjem Talvy et al. (2000). The dependence of the approach velocity on the separation distance, as well as the swaying of the trailing Taylor bubble tip while approaching the leading one, can be related to the measured flow field in the wake of the leading bubble.

Acknowledgements

This work was supported by a grant from the Israel Science Foundation. The authors gratefully acknowledge this support.

References

Adrian, R.J., 1991. Particle-imaging techniques for experimental fluid mechanics. Annu. Rev. Fluid Mech. 23, 261–304.

Ahmad, W.R., DeJesus, J.M., Kawaji, M., 1998. Falling film hydrodynamics in slug flow. Chem. Eng. Sci. 53, 123–130.

Aladjem Talvy, C., Shemer, L., Barnea, D., 2000. On the interaction between two consecutive elongated bubbles in a vertical pipe. Int. J. Multiphase Flow 26, 1905–1923.

DeJesus, J.D., Ahmad, W., Kawaji, M., 1995. Experimental study of flow structure in vertical slug flow. In: Proceedings of the Second International Conference on Multiphase Flow'95 – Kyoto, Kyoto, Japan, vol. 4, Session p9, pp. 51–55.

Fabre, J., Grenier, P., Gadoin, E., 1993. Evolution of slug flow in long pipe. In: Sixth International Conference On Multiphase Production, Cannes, France. BHR Group Conference Series, vol. 4, pp. 165–177.

Fagundes Netto, J.R., Fabre, J., Grenier, P., Péresson, L., 1998. An experimental study of an isolated long bubble in an horizontal liquid flow. In: Third International Conference on Multiphase Flow, ICMF'98, Lyon, France, June 8–12.

Kawaji, M., DeJesus, J.M., Tudose, G., 1997. Investigation of flow structures in vertical slug flow. Nucl. Eng. Des. 175, 37–48.

Kvernvold, O., Vindøy, V., Søntvedt, T., Saasen, A., Selmer-Olsen, S., 1984. Velocity distribution in horizontal slug flow. Int. J. Multiphase Flow 10, 441–457.

Laufer, J., 1953. The structure of turbulence in fully developed pipe flow. NACA Report 1174.

Moissis, R., Griffith, P., 1962. Entrance effects in a two-phase slug flow. J. Heat Transfer 84, 366–370.

Nakoryakov, V.E., Kashinski, O.N., Kozmenko, B.K., 1986. Experimental study of gas–liquid slug flow in a small-diameter vertical pipe. Int. J. Multiphase Flow 12, 337–355.

Nakoryakov, V.E., Kashinski, O.N., Petukhov, A.V., Gorelik, R.S., 1989. Study of local hydrodynamic characteristics of upward slug flow. Exp. Fluids 7, 560–566.

Pinto, A.M.F.R., Campos, J.B.L.M., 1996. Coalescence of two gas slugs rising in a vertical column of liquid. Chem. Eng. Sci. 51, 45–54.

Polonsky, S., Barnea, D., Shemer, L., 1999a. Averaged and time-dependent characteristics of the motion of an elongated bubble in a vertical pipe. Int. J. Multiphase Flow 25, 795–812.

Polonsky, S., Shemer, L., Barnea, D., 1999b. The relation between the Taylor bubble motion and the velocity field ahead of it. Int. J. Multiphase Flow 25, 957–975.

Roth, G.I., Katz, J., 1999. Parallel truncated multiplication and other methods for improving the speed and accuracy of PIV calculations. In: Proceedings of the Third ASME/JSME Joint Fluids Eng. Conference FEDSM99-6998, San Francisco, CA.

Shemer, L., Barnea, D., 1987. Visualization of the instantaneous velocity profiles in gas–liquid slug flow. PhysicoChem. Hydrodyn. 8, 243–253.

Taylor, A.M.K.P., Whitelaw, J.H., 1984. Velocity characteristics in the turbulent near wakes of confined axisymmetric bluff bodies. J. Fluid Mech. 139, 391–416.

Tokuhiro, A., Maekawa, M., Iizuka, K., Hishida, K., Maeda, M., 1998. Turbulent flow past a bubble and an ellipsoid using shadow-image and PIV techniques. Int. J. Multiphase Flow 24, 1383–1406.

van Hout, R., Barnea, D., Shemer, L., 2001. Evolution of statistical parameters of gas-liquid slug flow along vertical pipes. Int. J. Multiphase Flow 27, 1579–1602.